Sampling effect on contact and transport properties between fractal surfaces

Christophe Vallet, Didier Lasseux, H. Zahouani, Philippe Sainsot

Sampling effect on contact and transport properties between fractal surfaces

C. Vallet [*,a], D. Lasseux [*,b], H. Zahouani [d], P. Sainsot [c]

[a] *EDF R&D, avenue des Renardières - Ecuelles, 77818 Moret-sur-Loing Cedex, France*

[b] *TREFLE, CNRS UMR8508, Esplanade des Arts et Métiers, 33405 Talence Cedex, France*

[c] *LaMCoS, INSA-Lyon, CNRS UMR5259, F69621, France*

[d] *ENISE, 58 rue Jean Parot, 42000 Saint Etienne, France*

Abstract

In this work, we are interested in the contact between a self-affine fractal surface pressed against a smooth and perfectly rigid plane. The purpose is to analyse the influence of both sampling interval Δ and sampling length L, on the determination of surface roughness parameters, contact areas and viscous and diffusive flow through the aperture field resulting from the contact under load. To accomplish this analysis, fractal surfaces used in this work are obtained from numerical simulations. Models for synthesizing a fractal surface, computing mechanical deformation of asperities as well as determining viscous and diffusive flow are briefly presented. At the macroscopic scale, viscous and diffusive flow are fully characterized by the transmissivity $\mathbf{K}$ and effective diffusivity $\mathbf{D}$ tensors respectively. Results show that fractal dimension D_f and arithmetic roughness Ra are almost insensitive to Δ and L under conditions that are discussed. Contact areas are invariant whatever L and become increasingly sensitive to Δ while decreasing the arithmetic roughness Ra. The impact of L and Δ in the determination of transport properties also increases when $\mathbf{K}$ and $\mathbf{D}$ decrease, i.e. for small Ra and large average contact pressure Pca.

Key words: Self-affine fractal surfaces, Rough contact, Transport properties, Sampling parameters

* Corresponding author
Email addresses: christophe.vallet@edf.fr (C. Vallet), didier.lasseux@bordeaux.ensam.fr (D. Lasseux).

Article published in Tribology International 42 (2009) 1132-1145

1 Introduction

In the past decades, many works, both numerical and experimental, have been devoted to the study of fluid flows through fractures in rocks [1–3]. This subject takes many practical applications in water supply, petroleum extraction or long-term nuclear waste storage. In mechanical design, fluid flow through the contact between machined surfaces have received interest mainly in the context of tribological problems, especially in the understanding of lubrication mechanisms, like in the design of ball bearings or gear drives [4]-[5]. In those applications, surfaces in contact are generally in relative motion, leading to friction and wear problems.

Here, we are interested in fluid flow through motionless rough surfaces pressed against each other. This problem is of great interest in many industrial applications, like in design and safety of nuclear power plants or cryotechnic rocket engines, where sealing of some units is made by a direct contact between metallic surfaces [6]. Even under tightening, contact only occurs locally at the top of asperities and spaces left between surfaces form a connected aperture field which allows fluid flow through the contact. In this work, we study viscous and diffusive flows through the aperture field formed by a rough surface pressed against a perfectly rigid and smooth plane. In a companion paper [7], Vallet et al. have presented a deterministic approach to estimate transport properties from initial surface roughness, i.e. intrinsic parameters relating the fluid flux to the driving force, for both viscous flow and diffusion, taking into account surface flattening due to tightening. Moreover, they have shown that real surfaces obtained by a random process, like lapping or sand-blasting, can be consistently represented by synthetic self-affine fractal surfaces, both from the mechanical contact and transport properties points of view. The aim of this paper is to investigate the influence of sampling variables describing the rough surface on the determination of roughness parameters, contact areas and transport properties. In their work, Nguyen et al. [8] have studied the influence of the sampling conditions in the estimation of a so-called Birmingham set of parameters [9]. Here, rough surfaces under investigation exhibit fractal properties as in [7] and are obtained from numerical simulation.

The choice of sampling variables arises while measuring a real surface and the goal of this work is to contribute to the determination of optimal measuring parameters. Indeed, surface scanning is a delicate process because it leads to surface digitizing and hence to information loss. Many measuring instruments are commonly used (see [9]), based on contact or non-contact techniques, and their choice mainly depends on surface topography as well as scales under consideration. Roughness of machined surfaces like lapped or sand-blasted surfaces is composed of a wide range of frequencies, varying from body dimensions to interatomic distances. However, whatever the measuring method,

only a range of frequencies is captured, the lowest frequency being imposed by the scanning length and the largest by the sampling interval or scanning resolution. To keep a reasonable amount of data, a compromise between scanning resolution and scanning length must also be made.

In section 2, we briefly recall models to synthesize a self-affine fractal surface, to compute surface deflections in elasto-perfectly plastic regime and to determine fluid transport properties through a rough contact. For more details on the models, the reader is invited to refer to [7]. Section 3 is dedicated to the analysis of the effects of sampling variables, i.e. sampling interval and sampling length, on surface roughness parameters, contact areas and transport properties, for an average contact pressure ranging from 10 to 600 MPa. To accomplish this analysis, four reference surfaces are first synthesized with different roughness parameters. The analysis of the sampling interval effect is performed by resampling each reference surface with three different sampling intervals, without changing the sampling length. In the same way, the sampling length effect is studied by resizing each reference surface with three different lengths, keeping the initial sampling interval constant. Finally, main conclusions are collected in section 4.

2 Models

2.1 Fractal surface synthesizing model

Fractal concept was first mentioned by Mandelbrot [10]. His observations showed that the length of a natural coastline does not converge but increases monotonically when decreasing the unit of measurement. This concept was used to describe many irregular shapes like mountains, coastlines or fractured surfaces that Euclidian geometry cannot properly describe.
From a mathematical point of view, a fractal surface is shown to be self-affine, which means that the surface appears similar under various degrees of magnification (see fig. 1) with scaling magnification that is direction dependent. The power spectrum $P(\omega_x, \omega_y)$ and the structure function $\delta(\tau_x, \tau_y)$ of this kind of surfaces follow power laws. For an isotropic self-affine fractal surface $z\,(x, y)$, they are given by [11]:

$$P(\omega_x, \omega_y) \propto \left|\widetilde{Z}(\omega_x, \omega_y)\right|^2 \propto \frac{1}{\omega_{eq}^{8-2D_f}} \tag{1}$$

where $\widetilde{Z}(\omega_x, \omega_y)$ is the Fourier transform of $z\,(x, y)$ and $\omega_{eq} = \sqrt{\omega_x^2 + \omega_y^2}$;

$$\delta(\tau_x, \tau_y) = \left\langle [z(x + \tau_x, y + \tau_y) - z(x, y)]^2 \right\rangle \propto \tau_{eq}^{6-2D_f} \tag{2}$$

where $\tau_{eq} = \sqrt{\tau_x^2 + \tau_y^2}$.
In these equations, D_f is called the fractal dimension and for a surface "in space", $2 < D_f < 3$. This parameter is related to the relative power of frequency content, which means that the larger D_f the more irregular the surface. Practically, D_f can be determined from the slope of $log(P) = f(log\ \omega_{eq})$ or $log(\delta) = f(log\ \tau_{eq})$ plots. In section 3, fractal dimensions will be determined from the structure function δ for practical arguments that will be clearly exposed.

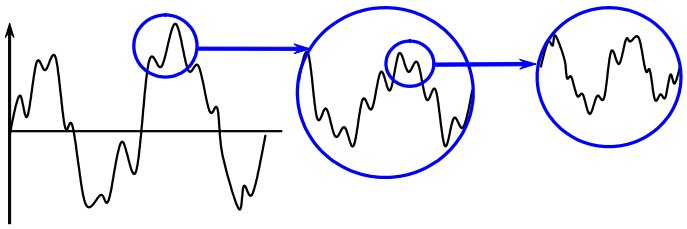

Fig. 1. Self-affine profile -

To perform our analysis, self-affine fractal surfaces are synthesized from their power spectrum (eq. (1)) following an approach based on the Fourier filtering method [11]. A random pattern a_{mn} ($1 \leq m \leq n_x$ and $1 \leq n \leq n_y$) is first generated in the physical space. A correlation among the Fourier coefficients $\tilde{a}_{kl}$ of a_{mn} is introduced such that moduli of $\tilde{z}_{kl}$ follow a power law as given by equation (1):

$$\tilde{z}_{kl} = \frac{\tilde{a}_{kl}}{(\omega_{kl})^{4-D_f}} \tag{3}$$

where $\omega_{kl} = 2\pi\sqrt{\left(\frac{k}{L_x}\right)^2 + \left(\frac{l}{L_y}\right)^2}$, L_x and L_y being the surface dimensions in two orthogonal x and y directions respectively.

The fractal surface z_{mn} is then obtained by a discrete inverse Fourier transform of $\tilde{z}_{kl}$:

$$z_{mn} = \frac{1}{n_x n_y} \sum_{k=0}^{n_x-1} \sum_{l=0}^{n_y-1} \tilde{z}_{kl} e^{\left(\mathrm{i}k\frac{2m\pi}{n_x} + \mathrm{i}l\frac{2n\pi}{n_y}\right)} \tag{4}$$

Finally, a rescaling is performed on z_{mn} to obtain the desired arithmetic roughness Ra:

$$\bar{z}_{mn} = \frac{Ra}{\frac{1}{n_x n_y} \sum_{k=1}^{n_x} \sum_{l=1}^{n_y} |z_{kl}|} z_{mn} \tag{5}$$

2.2 Elasto-plastic deformation model

When two rough surfaces are put in contact, effective contact occurs at discrete spots, involving stresses that equilibrate the applied load. Resolution of rough contact problem has received much interest in the past decades and a review of the main methods employed for this resolution can be found in [12]. Statistical approaches, initially developed by Greenwood and Williamson [13] and then modified by many authors [14–17], yield important qualitative results concerning the effect of statistical roughness parameters on the true contact area. However, due to the multiscale nature of rough surfaces, it has been observed that roughness parameters used in these models strongly depend on sampling variables describing rough surfaces [18]. Thus, these statistical models often provide erroneous results from a quantitative point of view. With the advance of computer capabilities, numerical and deterministic models have been developed, allowing the use of digitized real surfaces without any assumption on height distribution. However, the grid used to discretize the surface must be as fine as possible to capture the micro-roughness, and in the same time, large enough to include longer wavelengths. These two constraints imply a large number of data, causing numerical difficulties to solve 3D contact problems with classical methods, such as finite element methods (FEM). An alternative technique applied to the contact between fractal surfaces was employed by Willner [19], following a previous work of Tian and Bhushan [20]. This technique is based on the minimization of the total complementary potential energy using a variational approach and the Boussinesq solution for semi-infinite bodies. Other fast methods, based on multilevel technique or fast Fourier transform (FFT), have been developed and in this paper, we use a numerical procedure based on the work of Sainsot et al. [21] to solve the contact problem. In this model, only normal effects are considered and contact bodies are assumed to be semi infinite. This last assumption, valid for a small contact area compared to body dimensions and for asperities having small slopes, allows the derivation of a direct relationship between surface deflections and contact pressures:

$$u\left(\mathbf{x}\right) = \int_{S} U\left(\mathbf{x}, \xi\right) p^{c}\left(\xi\right) dS \tag{6}$$

Here $u\left(\mathbf{x}\right)$ is the surface deflection at point $\mathbf{x}\left(x, y\right)$ on the surface S, $U\left(\mathbf{x}, \xi\right)$ is the deflection at $\mathbf{x}$ due to a unit load at $\xi\left(\xi_x, \xi_y\right)$ while $p^{c}\left(\xi\right)$ designates the contact pressure at ξ and S the apparent contact surface. From this equation, it appears that only surface deflections have to be computed (and not the displacements in the bulk), reducing drastically the system of equations to be solved.

When solids are elastic and homogeneous, the influence coefficient $U\left(\mathbf{x}, \xi\right)$ can

be expressed by the method of potentials proposed by Boussinesq [22]:

$$U(\mathbf{x},\xi) = \frac{1-\nu^2}{\pi E}\frac{1}{\sqrt{(x-\xi_x)^2+(y-\xi_y)^2}} \tag{7}$$

where E is the Young's modulus and ν the Poisson ratio of the surface material under consideration.

To satisfy the overall equilibrium, local contact pressures must also verify:

$$\frac{1}{S}\int_S p^c(\mathbf{x})\,dS = \mathrm{Pca} \tag{8}$$

where Pca is the average applied contact pressure.

The detailed procedure to solve this problem is given in [23]. To take into account plastic deformation, a plastic criterion is directly applied on contact pressures. Materials are assumed to follow an elastic-perfectly plastic behavior, i.e. contact pressures are bounded by the hardness $\mathcal{H}$ of the softer material.

2.3 Fluid transport models

2.3.1 Viscous flow and diffusion at the micro-scale

In this section, we consider incompressible, isothermal and stationary mass transfers due to viscous flow on the one hand and to diffusion on the other. At the micro-scale, viscous creeping flow (at small Reynolds number) through a rough fracture can be described by the Stokes model and diffusion by Fick's law. If we assume that the aperture field $h(x,y)$ is slowly varying, i.e. that slopes of asperities are small, the two previous models can be reduced from 3D to 2D. This can be performed using an order of magnitude analysis and an integration of the balance equations in the direction normal to the mean plane of the contact (z-direction) [7]. In these circumstances, viscous flow is described by the Reynolds model:

$$\mathbf{q}_v = -\frac{h^3}{12\mu}\nabla p \ \text{ in } \beta \tag{9a}$$

$$\nabla.\mathbf{q}_v = 0 \ \text{ in } \beta \tag{9b}$$

$$\mathbf{q}_v.\mathbf{n} = 0 \ \text{ on } C_{\beta\sigma} \tag{9c}$$

In these equations, β designates the fluid phase and σ the region of contours $C_{\beta\sigma}$ where effective contact occurs in the x-y plane (see fig. 2); $\mathbf{q}_v = \int_0^h \mathbf{v}dz$ is the volume flow rate of the β-phase per unit width, $\mathbf{v}$ and p are the velocity and pressure in the β-phase of dynamic viscosity μ.

In the same way, the diffusion problem becomes:

$$\mathbf{q}_d = -\mathcal{D}h\nabla c \ \text{ in } \beta \tag{10a}$$

$$\nabla.\mathbf{q}_d = 0 \ \text{ in } \beta \tag{10b}$$

$$\mathbf{q}_d.\mathbf{n} = 0 \ \text{ on } C_{\beta\sigma} \tag{10c}$$

Here $\mathbf{q}_d = \int_0^h \mathbf{j} dz$, $\mathbf{j}$ being the diffusive flux, c the concentration of the species which diffuses through the contact and $\mathcal{D}$ the molecular diffusion coefficient.

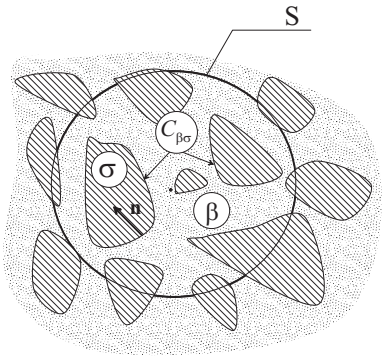

Fig. 2. Local contact configuration. σ designates the region where effective contact occurs within S while β represents the fluid phase -

2.3.2 Transport properties of the rough contact

Equations (9) and (10) are formally identical. They can be rewritten in a generic form:

$$\mathbf{q} = -k\nabla\omega \ \text{ in } \beta \tag{11a}$$

$$\nabla.\mathbf{q} = 0 \ \text{ in } \beta \tag{11b}$$

$$\mathbf{q}.\mathbf{n} = 0 \ \text{ on } C_{\beta\sigma} \tag{11c}$$

with $k = \frac{h^3}{12\mu}$ and $\omega = p$ for viscous flow and $k = \mathcal{D}h$ and $\omega = c$ for diffusion.

By averaging these equations over a small portion S of the contact, the previous model can be up-scaled from micro to macro-scale. This operation allows to derive macroscopic models of transport relating the macroscopic flow rate at the scale of S, to the macroscopic driving force (i.e. the macroscopic pressure gradient or species gradient). Moreover, it provides an explicit way to determine the transport coefficients appearing in these macroscopic models. The averaging process is similar to volume averaging [24] and is based on the definitions of the two operators applied on any quantity φ:

$$\langle\varphi\rangle = \frac{1}{S}\int_{S_\beta}\varphi dS = \frac{1}{S_\beta + S_c}\int_{S_\beta}\varphi dS \tag{12a}$$

and

$$\langle\varphi\rangle^{\beta} = \frac{1}{S_{\beta}}\int_{S_{\beta}}\varphi dS \tag{12b}$$

along with the averaging theorem:

$$\langle\nabla\varphi\rangle = \nabla\langle\varphi\rangle + \frac{1}{S}\int_{C_{\beta\sigma}}\mathbf{n}\varphi dS \tag{12c}$$

Using a procedure employed for similar problems [25]-[26], it can be shown that the generic macroscopic model takes the form:

$$\langle\mathbf{q}\rangle = -\mathbf{H}.\nabla\langle\omega\rangle^{\beta} \tag{13a}$$

$$\nabla.\langle\mathbf{q}\rangle = 0 \tag{13b}$$

In equation (13a), the tensor $\mathbf{H}$ can be explicitly determined from the aperture field according to:

$$\mathbf{H} = \langle k\left(\mathbf{I} + \nabla\mathbf{b}\right)\rangle \tag{14}$$

where $\mathbf{b}$ is solution of the closure problem that is written as:

$$\nabla.\left(k\nabla\mathbf{b}\right) = -\nabla\widetilde{k} \text{ in } \beta \tag{15a}$$

$$-\mathbf{n}_{\beta\sigma}.\nabla\mathbf{b} = \mathbf{n}_{\beta\sigma} \text{ on } C_{\beta\sigma} \tag{15b}$$

$$\mathbf{b}\left(\mathbf{x} + \mathbf{r}_i\right) = \mathbf{b}\left(\mathbf{x}\right) \tag{15c}$$

$$\langle\mathbf{b}\rangle = 0 \tag{15d}$$

In the above equations, $\widetilde{k} = k - \langle k\rangle$ and $\mathbf{r}_i$ is the surface element dimension in the i^{th} direction. This surface element is supposed to be representative of a periodic infinite structure.

For viscous flow, the flow rate per unit width of the contact, at the scale of the surface element, is hence:

$$\langle\mathbf{q}_v\rangle = -\frac{\mathbf{K}}{\mu}.\nabla\langle p\rangle^{\beta} \tag{16a}$$

$$\nabla.\langle\mathbf{q}_v\rangle = 0 \tag{16b}$$

where $\mathbf{K} = \mathbf{H}$ is the transmissivity tensor with $k = \frac{h^3}{12}$ in (14) and (15). It must be noted that $\mathbf{K}$ has the dimension of cubic length.

In the same way, the flow rate per unit contact width resulting from diffusion at the scale of the surface element is given by:

$$\langle\mathbf{q}_d\rangle = -\mathcal{D}\mathbf{D}.\nabla\langle c\rangle^{\beta} \tag{17a}$$

$$\nabla . \langle \mathbf{q}_d \rangle = 0 \tag{17b}$$

where $\mathbf{D} = \mathbf{H}$ is the effective diffusivity tensor with $k = h$ in (14) and (15). Note that $\mathbf{D}$ has the dimension of length.

Both $\mathbf{K}$ and $\mathbf{D}$ are intrinsic, i.e. they can be estimated from the aperture field h at a given load as indicated in the following section.

2.4 Computational algorithm

The deterministic approach employed to determine true contact areas and transport properties $\mathbf{K}$ and $\mathbf{D}$ of a rough contact is shown in figure 3. It begins with a set of n_x x n_y points describing a rough surface $\overline{z}(x, y)$ synthesized from the method described above. The aperture field $\overline{h}(x, y)$ resulting from deformation of the initial rough surface $\overline{z}(x, y)$ is computed using the elastic-perfectly plastic model as indicated in section 2.2. Intrinsic transmissivity and diffusivity tensors, $\mathbf{K}$ and $\mathbf{D}$ respectively, are computed using the same numerical procedure. Distinction between viscous and diffusive transport is performed in the surface preparation module. The percolation module allows to remove from $\overline{h}(x, y)$ all the non-percolating clusters, i.e. non-contact areas not connected to surface edges.

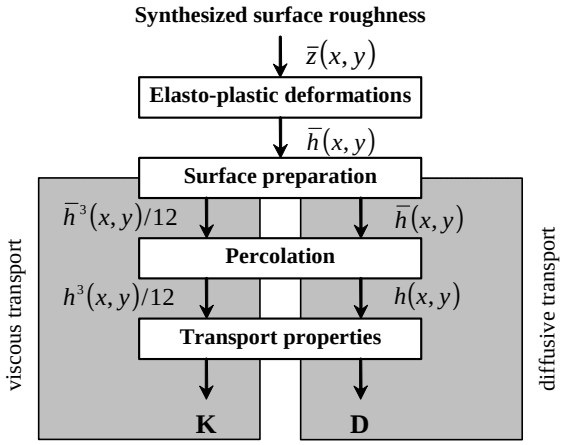

Fig. 3. Computational algorithm flowchart -

3 Effects of sampling variables on surface roughness parameters, contact areas and transport properties

In this section, we consider four reference fractal surfaces characterized by a fractal dimension $D_f \in \{2.3 \ ; \ 2.7\}$ and an arithmetic roughness $Ra \in \{0.1$

μm ; 1 $\mu m\}$ (see tab. 1). Each surface is synthesized from the same random pattern a_{mn} and with the same sampling variables, i.e. a length L of 2 mm sampled with $n = 1024$ points corresponding to a sampling interval Δ of 1.95 μm. These surfaces represent our basic data that can be considered as extracted from direct measurements of real surfaces as shown by the analysis in [7]. Each surface element is considered as representative of a larger real surface. Ranges of variation of D_f and Ra were chosen in agreement with measurements made on engineering surfaces [18]-[27]. In [7], it was shown that some machined surfaces (like lapped surfaces) can exhibit fractal properties at high frequencies only, and this can be simulated by introducing a cut-off frequency ω_c during the synthesizing process. In that case, $P(\omega)$ is taken as a constant for $\omega < \omega_c$ (see [7]-[28]). To guarantee that reference surfaces are not fractal at scales larger than their own size, i.e. that sampling lengths were chosen large enough, surfaces were synthesized with a cut-off frequency $\omega_c = 12\pi\ rad.mm^{-1}$ (see tab. 1). This has also the advantage of ensuring a perfect isotropy of the transport properties (see [7]).

Table 1
Surface parameters -

	Sampling length L **x** L (mm)	**Sampling** n **x** n (pts)	Ra (μm)	D_f	ω_c $(rad.mm^{-1})$
surface 1	2 x 2	1024 x 1024	**0.1**	**2.3**	12π
surface 2			**1.0**	**2.3**	
surface 3			**0.1**	**2.7**	
surface 4			**1.0**	**2.7**	

In the following, the contact is assumed to be made of a stainless steel rough surface, which mechanical properties are given in table 2, pressed against a smooth and perfectly rigid plane parallel to the mean plane of the rough surface. As indicated in section 2.2, the deformation of asperities resulting from the applied load can be locally in the elastic or plastic regime depending on the local contact pressure.

Table 2
Mechanical properties of stainless steel -

Young modulus E	Poisson ratio ν	Hardness $\mathcal{H}$
210 GPa	0.3	1800 MPa

3.1 Effect of sampling interval Δ

The aim of this paragraph is to study the influence of the sampling interval $\Delta = L/n$ on roughness parameters on the one hand, and contact areas and transport properties on the other. It is accomplished by under-sampling each reference surface using 512 x 512, 256 x 256 and 128 x 128 points, which correspond to sampling intervals $\Delta = 3.91\ \mu m$, $\Delta = 7.81\ \mu m$ and $\Delta = 15.62\ \mu m$ respectively. This is achieved by keeping the sampling length L constant equal to 2 mm while successively considering 1 point over 2, 4 and 8 from the original reference surfaces respectively.

3.1.1 Fractal dimension and arithmetic roughness

As already mentioned, the fractal dimension of rough surfaces is determined from their structure function δ. This choice is motivated by several arguments. As pointed out by Ganti and Bhushan [27], the power spectrum is inaccurate when applied to discrete functions due to the approximation of the frequency content. Since we are analyzing the effect of sampling, inaccuracy is expected to increase when Δ increases, in particular at high frequencies that are mainly altered while under-sampling. In our case, this is a major drawback since the presence of the frequency cut-off ω_c would require the characterization of the fractal dimension D_f from the higher frequency content of the surface. Moreover, for surfaces investigated here, synthesized from a random pattern, the scatter on the structure function is much smaller than that on the power spectrum, leading to a more precise estimation of D_f from δ. In addition, the computation of δ is simpler to implement for practical use in engineering. Consequently, D_f is estimated from the slope of the $log(\delta) = f(log\ \tau_{eq})$ plot, for each under-sampled surface and for τ_{eq} varying from Δ to $\frac{L}{2}$. As can be seen from equation (2), the slope of the structure function log-plot does not depend on Ra, since changing Ra only leads to a rescaling of heights and hence to a vertical shift of this plot. As a consequence, estimations of D_f on surfaces 1 and 2 on the one hand, and on surfaces 3 and 4 on the other, are strictly identical.
In figures 4 and 5, we have represented in dashed lines the structure function plots $log(\delta) = f(log\ \tau_{eq})$ for the two pairs of surfaces {1, 2} and {3, 4} respectively, for each sampling interval Δ. To show the influence of ω_c on δ, structure functions of fractal surfaces synthesized without any cut-off frequency ($\omega_c = 0$ $rad.mm^{-1}$) have also been reported as solid lines in these figures. Fractal dimensions D_f, estimated from least squares fits on the linear part of these plots, are reported in table 3.
First, it can be seen on figures 4 and 5 that the presence of ω_c alters the structure function linearity, even at values of the lag τ_{eq} smaller than $\frac{2\pi}{\omega_c} = \frac{1}{6}$

mm. Results in table 3 clearly show, as expected, that D_f is not appreciably sensitive to Δ, especially for $\omega_c = 0$. In that case, the increase on the estimated value of D_f is only 0.4% with respect to the reference surface when Δ is multiplied by 8. For $\omega_c = 12\pi\ rad.mm^{-1}$, D_f seems to increase slightly with Δ (4 to 5% of increase with respect to the reference surface while multiplying Δ by 8). This behavior can be explained as follows. Increasing Δ leads to a truncation of δ at small values of τ_{eq}. For $\omega_c = 0\ rad.mm^{-1}$, δ remains linear over nearly the whole investigated range of τ_{eq}. In this case, the truncation has also no influence on the estimation of D_f. Note that the non-linearity of $log(\delta) = f(log\ \tau_{eq})$ at large values of τ_{eq} is only due to a finite size effect. For large values of τ_{eq}, the estimation of δ is not precise since there is not enough information. For $\omega_c = 12\pi\ rad.mm^{-1}$, δ is linear only for small values of τ_{eq} as indicated above. For this reason, information contained in δ becomes insufficient at small values of τ_{eq} to determine D_f when Δ is increased. From a practical point of view, this suggests that the sampling interval Δ must be kept smaller than a limit value in order to correctly capture the fractal property of such a surface. A thorough analysis, which is beyond the scope of this paper, would be necessary to provide quantitative results on this last feature. For Ra, calculation on each surface shows that this parameter is insensitive to under-sampling, in the range of Δ investigated here. As reported by Nguyen et al. [8], power spectra of machined surfaces, and more especially fractal surfaces, are dominated by low-frequency components, which means that long wavelengths have higher amplitude than short ones. As a consequence, the arithmetic roughness Ra also mainly depends on longer wavelengths. Since under-sampling does not affect long wavelengths, Ra is not significantly modified while increasing Δ.

Table 3
Effect of sampling interval Δ on fractal dimension D_f estimated from $log(\delta) = f(log\ \tau_{eq})$ of figures 4 and 5 -

	ω_c	Δ (μm)			
	($rad.mm^{-1}$)	1.95	3.91	7.81	15.62
Surfaces {1, 2}	0	2.33	2.33	2.32	2.34
	12π	2.33	2.35	2.38	2.45
Surfaces {3, 4}	0	2.67	2.67	2.67	2.68
	12π	2.63	2.65	2.68	2.74

3.1.2 Contact areas and transport properties

In the following, we study the effect of Δ on the estimation of the true contact area S_c and transport properties $\mathbf{K}$ and $\mathbf{D}$, while considering the four reference surfaces defined in table 1. In table 4, we have reported computational times

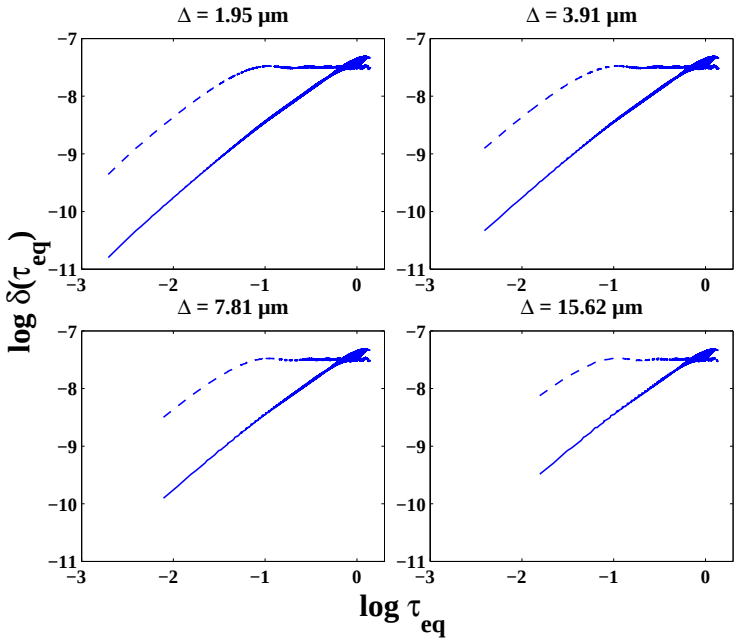

Fig. 4. Structure functions $\delta(\tau_{eq})$ of the under-sampled surfaces initially synthesized with $D_f = 2.3$. Solid lines: $\omega_c = 0\ rad.mm^{-1}$; dashed lines: $\omega_c = 12\pi\ rad.mm^{-1}$ -

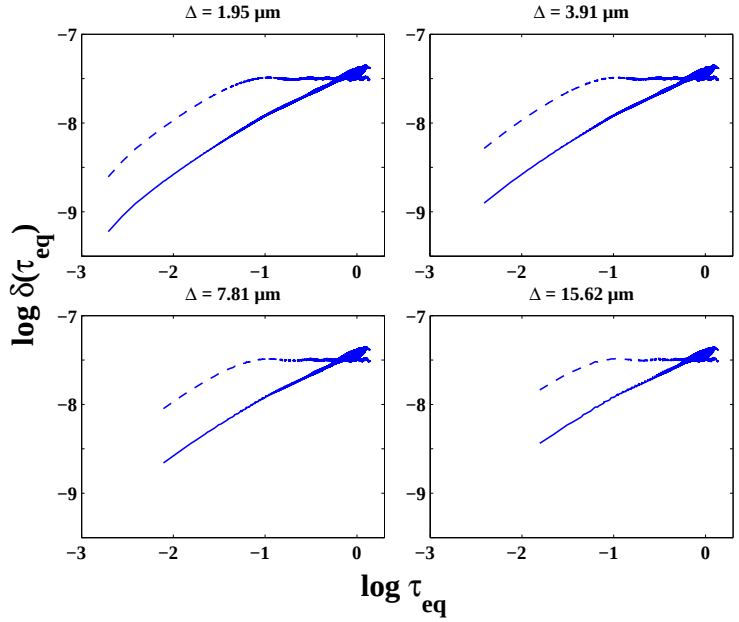

Fig. 5. Structure functions $\delta(\tau_{eq})$ of the under-sampled surfaces initially synthesized with $D_f = 2.7$. Solid lines: $\omega_c = 0\ rad.mm^{-1}$; dashed lines: $\omega_c = 12\pi\ rad.mm^{-1}$ -

required to run the whole algorithm schematized in figure 3, for each case under consideration and the whole range of Pca. Computations have been performed on a HP xw9300 workstation with a 2.4GHz AMD Dual Core processor. These data clearly illustrate the crucial issue of sampling since computational times roughly vary as n^2, from several hours for reference surfaces (1024 x 1024

points, i.e. $\Delta = 1.95\ \mu m$), to few minutes for 128 x 128 points, i.e. $\Delta = 15.62\ \mu m$. For practical use, this justifies the analysis reported below on the dependence of the true contact area S_c and transport properties **K** and **D** on sampling.

Table 4
Computational times -

	Surface 1	Surface 2	Surface 3	Surface 4
1024 x 1024 pts	68h	71h	60h	80h
512 x 512 pts	12h	11h	12h	13h
256 x 256 pts	1h10'	1h05'	1h45'	1h45'
128 x 128 pts	5'	15'	6'	8'

In figure 6, we have represented as dashed lines the influence of Δ on the ratio of the true contact area S_c to the apparent surface area $S = L^2$ versus the average contact pressure Pca. Pictures of contact areas of the corresponding reference surfaces are also represented for Pca = 600 MPa. In this figure, results on reference surfaces (solid lines) show that, whatever D_f, the larger Ra is, the smaller S_c/S for a given value of Pca. This indicates that the local contact pressure increases with Ra and, further, that the amount of contact spots experiencing plastic deformation is larger when Ra is large. This is in accordance with observations reported in [29]. Moreover, if we consider a trivial load-area relationship when the effective contact is entirely in the pure plastic regime, i.e. $S_c/S = Pca/\mathcal{H}$ [30], we find, for Pca = 600 Mpa, $S_c/S = 33.3\%$. This approximation is excellent for reference surfaces 2 and 4 ($Ra = 1\mu m$) confirming that a large amount of contact spots are resulting from plastic deformation for this value of Ra. On the contrary, for surfaces 1 and 3, this approximation underestimates S_c/S that is roughly 43% for surface 1 and 38% for surface 3 when Pca = 600 MPa, indicating that a significant amount of contact spots are supporting a contact pressure smaller than $\mathcal{H}$, i.e. are in the elastic regime. This is also in accordance with the fact that local contact spot areas are much smaller but more numerous when Ra is small (i.e. on surfaces 1 and 3) as shown in the insets of figure 6. In fact, there are three times more contact spots of size Δ^2 on surface 1 than on surface 2 although S_c/S_1 is only 25-30% larger than S_c/S_2. In addition, it can be noticed from the curves that S_c/S is much more sensitive to Δ for surfaces 1 and 3 than for surfaces 2 and 4, i.e. for smaller Ra. These observations can be explained as follows. When Ra is large (surfaces 2 and 4), S_c mainly results from effective contacts on large wavelength components of asperities that are also of larger amplitude. Small asperities, of short wavelength, are squashed leading to contact spots of relatively large area. Conversely, when Ra is small, contact occurs on asperities of high frequency of occurrence, leading to a high number of contact spots. While under-sampling, two cooperative effects are involved, explaining the contrast in the behavior of the dependence of

S_c/S upon Δ. First, under-sampling tends to smooth the surface, decreasing the highest detectable frequency. Second, it leads to an increase of the local contact spot area, simply due to the fact that, multiplying Δ by 2 for instance, multiplies the minimum contact spot area by 4. This effect is, of course, much less significant in situations involving large contact spot areas (i.e. when Ra is large).

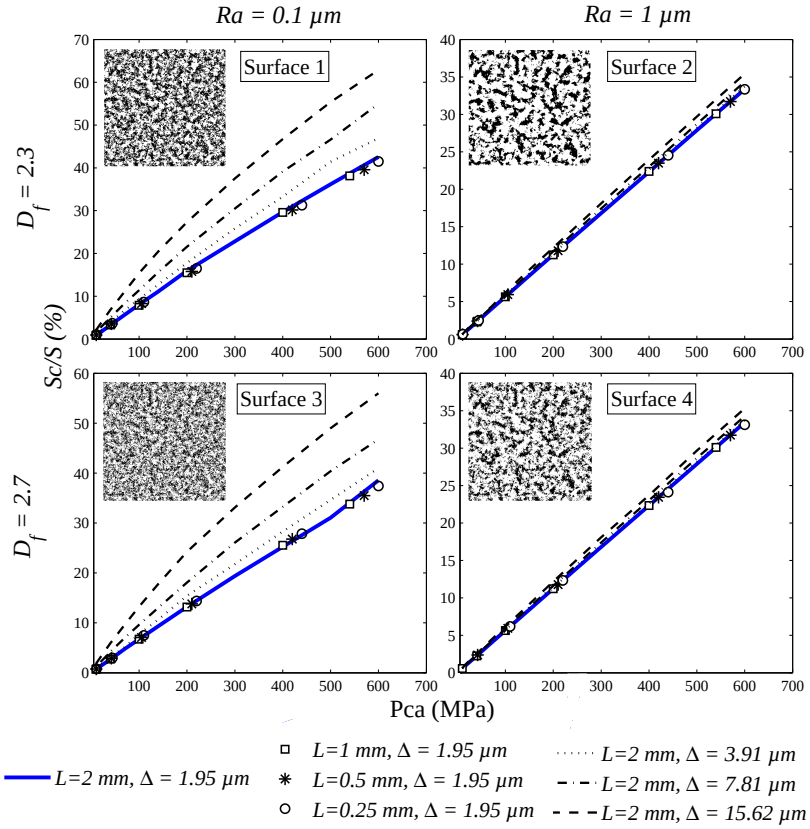

Fig. 6. Relative contact area S_c/S versus average contact pressure Pca. Insets: contact areas (dark spots) of the reference surfaces for Pca $= 600\ MPa$ -

In figures 7 and 8, all the diagonal terms of transmissivity $\mathbf{K}$ and effective diffusivity $\mathbf{D}$ tensors respectively are represented versus the average contact pressure Pca, for each sampling interval Δ. Off-diagonal terms of $\mathbf{K}$ and $\mathbf{D}$ are about two orders of magnitude smaller than diagonal ones and consequently, are not considered in our work. Transport properties of reference surfaces ($\Delta = 1.95\ \mu m$) appear as solid lines and representation was restricted to transmissivities and diffusivities respectively larger than $1e^{-9}\ \mu m^3$ and $1e^{-4}\ \mu m$. From these figures, it appears that the diagonal terms of $\mathbf{K}$ and $\mathbf{D}$ estimated on reference surfaces are identical confirming that synthesized surfaces are isotropic [7]. For large values of both Δ and Pca, a dispersion appears on diagonal terms. The origin of this behavior lies in the finite size effect of the element of surface under consideration which becomes more critical while increasing Pca. This finite size effect is such that the distribution of the

percolating cluster branches (i.e. connected paths where the fluid flows) that is statistically direction-independent for small values of Pca becomes increasingly direction-dependent while increasing Pca. Results on **K** and **D** indicate that these transport properties strongly depend on Ra and very little on D_f on the whole range of Pca investigated [31]. In addition, results of figures 7 and 8 clearly show that, for any given value of Pca, K_{xx}, K_{yy} and D_{xx}, D_{yy} decrease while increasing Δ and that this behavior is more significant on surfaces 1 and 3 ($Ra = 0.1\ \mu m$) than on surface 2 and 4 ($Ra = 1\ \mu m$). This can be simply explained while considering the results on the effective contact area presented above. While S_c increases with Δ, the mean aperture (and hence the transmissivity and diffusivity) decreases, this behavior being more significant when Ra is small. Note that under-sampling leads to an under-estimation of both **K** and **D**, and the under-estimation increases with Pca.

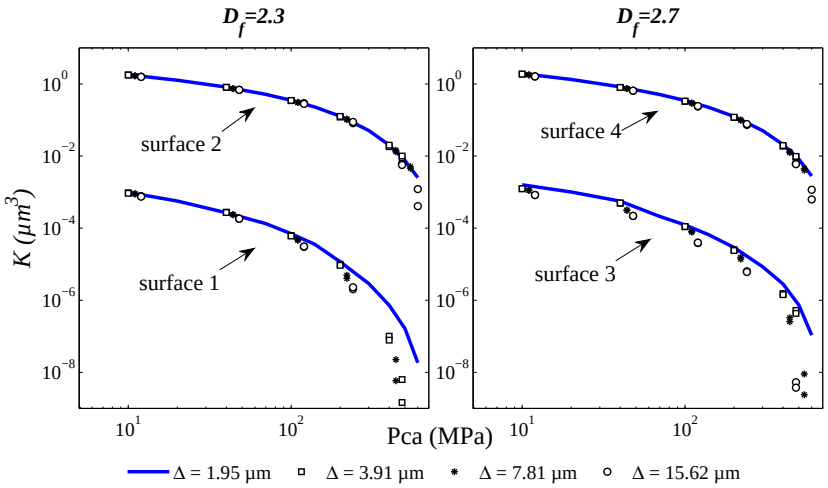

Fig. 7. Effect of sampling interval Δ on the diagonal terms of the transmissivity tensor K. The same symbols are used for the xx and yy components at each value of Δ -

To be more quantitative, we have represented in figures 9 and 10 the relative error on the transmissivity $\frac{\overline{K_r}-\overline{K}}{\overline{K_r}}$ and on the effective diffusivity $\frac{\overline{D_r}-\overline{D}}{\overline{D_r}}$ versus Pca for the three under-sampled surfaces. Here, $\overline{T}$ represents the mean value of diagonal terms of **T** while the subscript r refers to the reference surfaces. The relative error increases with Pca and Δ. Since $\overline{K}$ is always smaller than $\overline{K_r}$, relative error is bounded by 100%. For $\overline{K}$, it remains roughly smaller than 50-55% (leading to a factor 2 between $\overline{K}$ and $\overline{K_r}$) for Pca $\leq 100\ MPa$ for surfaces 1 and 3 and Pca $\leq 500\ MPa$ for surfaces 2 and 4 over the whole range of Δ. For $\overline{D}$, less than 50% of error is ensured for all values of Δ for Pca $\leq 200\ MPa$ for surfaces 1 and 3 and Pca $\leq 600\ MPa$ for surfaces 2 and 4. It must be noted that 50% of error remains reasonable compared to the range of variation of $\overline{K_r}$ and $\overline{D_r}$ and thinking to the practical measurement of these quantities [32].

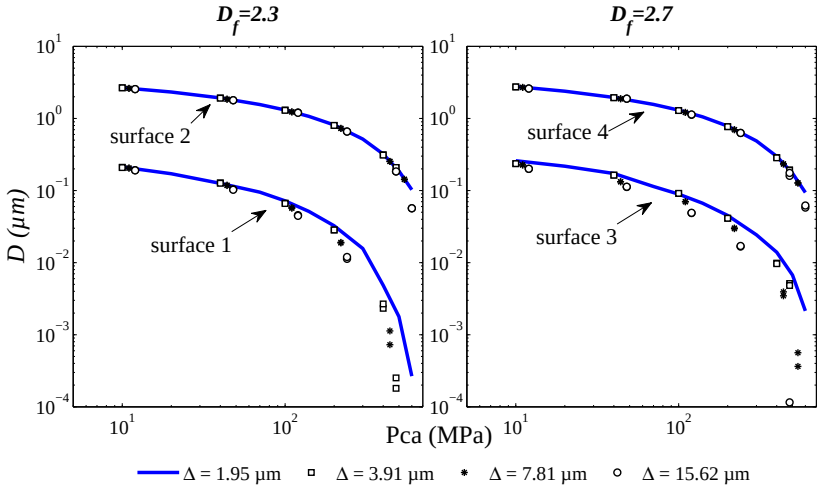

Fig. 8. Effect of sampling interval Δ on the diagonal terms of the diffusivity tensor D. The same symbols are used for the xx and yy components at each value of Δ -

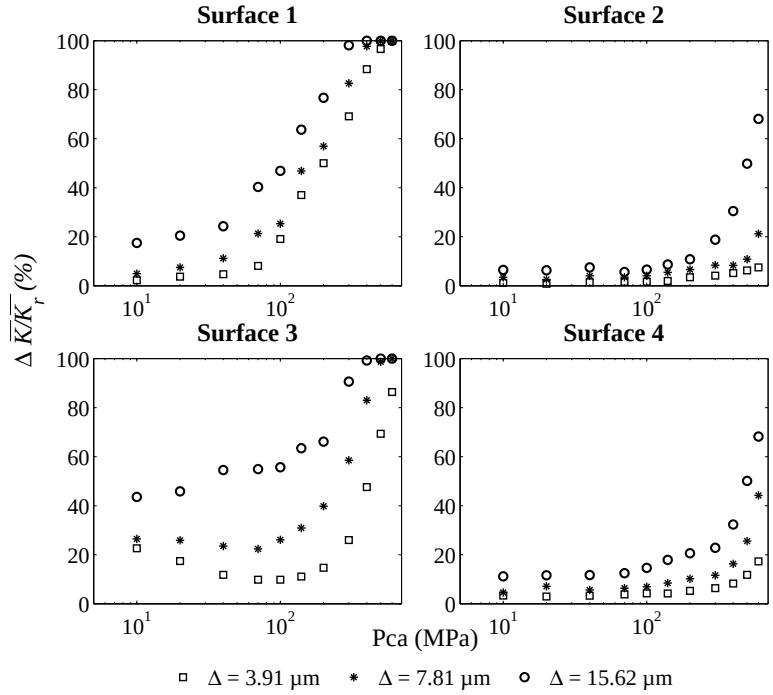

Fig. 9. Relative errors on K with respect to reference surfaces $\frac{\Delta\overline{K}}{\overline{K_r}} = \frac{\overline{K_r}-\overline{K}}{\overline{K_r}}$ for each sampling interval under consideration -

3.2 Effect of sampling length L

In this section, we are interested in the influence of the sampling length L on roughness parameters on the one hand, and contact and transport properties on the other. This study is performed by extracting three subdomains centered on each reference surface and having respective lengths $L = 1\ mm$, $L =$

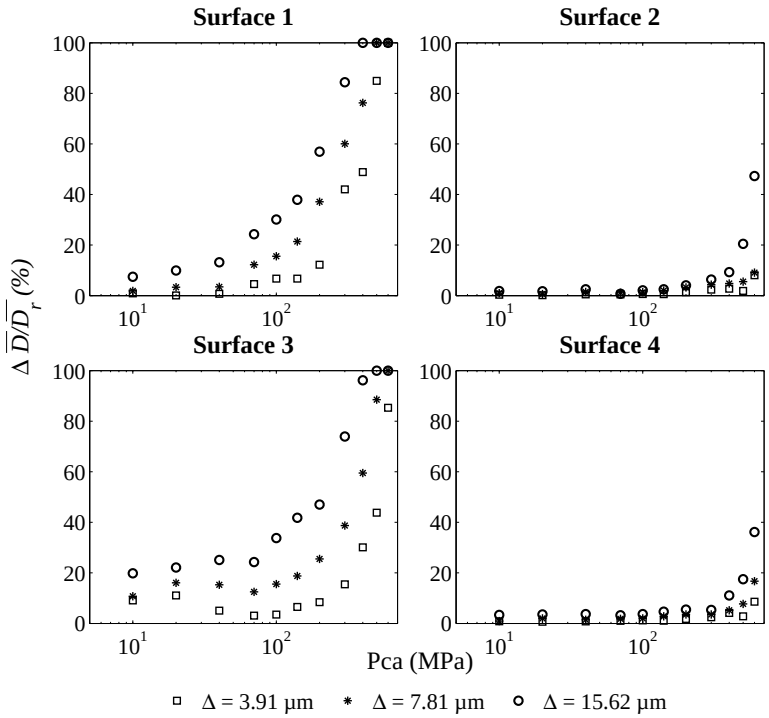

Fig. 10. Relative errors on D with respect to reference surfaces $\frac{\Delta\overline{D}}{\overline{D_r}} = \frac{\overline{D_r}-\overline{D}}{\overline{D_r}}$ for each sampling interval under consideration -

0.5 mm and $L = 0.25$ mm. These three subdomains are sampled with 512 x 512, 256 x 256 and 128 x 128 points respectively, keeping an identical sampling interval $\Delta = 1.95$ μm for each of them. It must be noticed that even for $L = 0.25$ mm, all scales of fractality are contained in the surface since ω_c corresponds to a wavelength of $\frac{1}{6}$ mm. The number of data points on these subdomains being identical to those used while under-sampling, computational times are also of the same order of magnitude as those reported in table 4.

3.2.1 Fractal dimension and arithmetic roughness

We begin with the investigation of the influence of L on the estimation of the surface parameters D_f and Ra. To highlight the influence of ω_c, we also report in this paragraph results on surfaces synthesized with $\omega_c = 0$. In figures 11 and 12, we have represented the $log(\delta) = f(log\ \tau_{eq})$ plots, for each surface under consideration here. In table 5, we have reported fractal dimensions estimated from least squares fits on these plots. It appears that, whatever ω_c, D_f is not sensitive to L in the range of sampling lengths investigated since errors remain smaller than 2%. Contrary to Δ, varying L does not induce any truncation of the linear part of δ. The estimation of D_f remains equally precise, even for small values of L.
Ratios of the arithmetic roughness Ra computed on each resized surface to the one of the reference surface Ra_r, are given in table 6. This table shows the effect

of ω_c. As explained previously, Ra mainly depends on longer wavelengths, and thus, it is generally L-dependent [8]. As expected for $\omega_c = 12\pi\ rad.mm^{-1}$, Ra is not sensitive to L in the investigated range of L, because the frequency content is not altered while resizing the surface.

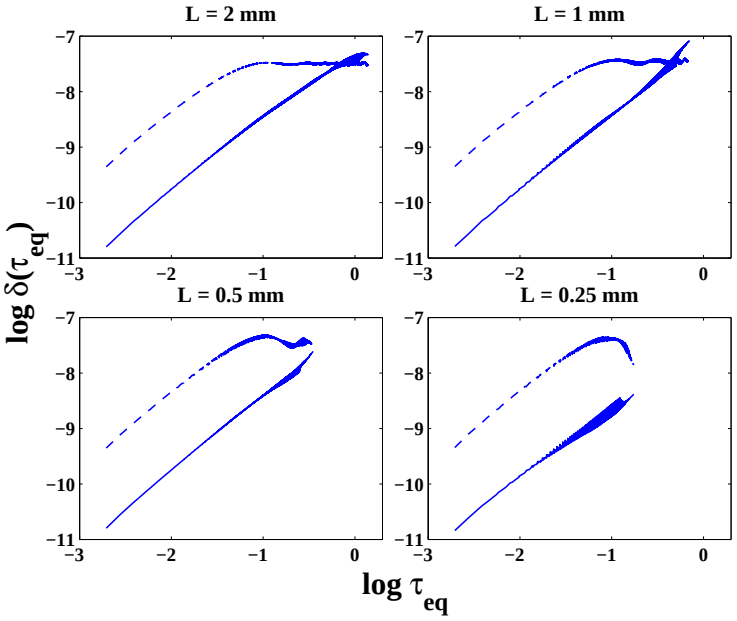

Fig. 11. Structure functions $\delta(\tau_{eq})$ of the resized surfaces, initially synthesized with $D_f = 2.3$. Solid lines: $\omega_c = 0\ rad.mm^{-1}$; dashed lines: $\omega_c = 12\pi\ rad.mm^{-1}$ -

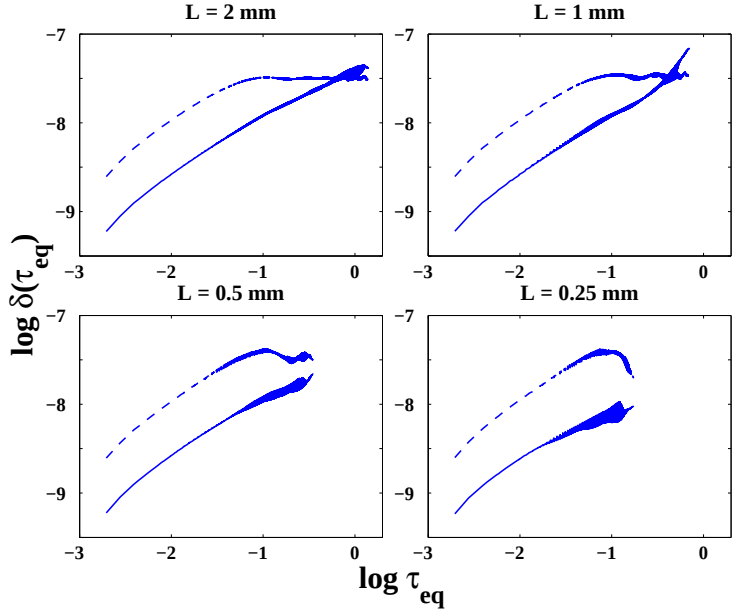

Fig. 12. Structure functions $\delta(\tau_{eq})$ of the resized surfaces, initially synthesized with $D_f = 2.7$. Solid lines: $\omega_c = 0\ rad.mm^{-1}$; dashed lines: $\omega_c = 12\pi\ rad.mm^{-1}$ -

Table 5
Effect of sampling length L on fractal dimension D_f -

	ω_c	L (mm)			
	$(rad.mm^{-1})$	2	1	0.5	0.25
Surfaces {1, 2}	0	2.33	2.30	2.31	2.34
	12π	2.33	2.33	2.32	2.33
Surfaces {3, 4}	0	2.65	2.66	2.65	2.67
	12π	2.65	2.66	2.65	2.64

Table 6
Effect of sampling length L on relative arithmetic roughness $\frac{Ra}{Ra_r}$ -

	ω_c	L (mm)			
	$(rad.mm^{-1})$	2	1	0.5	0.25
Surfaces {1, 2}	0	1.00	1.05	0.63	0.36
	12π	1.00	1.06	1.10	1.02
Surfaces {3, 4}	0	1.00	1.05	0.78	0.59
	12π	1.00	1.01	1.05	1.02

3.2.2 Contact areas and transport properties

The influence of L on the estimation of the ratio of the true contact area S_c to the apparent surface area $S = L^2$ versus the average contact pressure Pca is reported as symbols in figure 6. Whatever the reference surface, varying L has very little effect on the estimation of the true contact area. Maximum relative deviations occur at small contact pressure and remain smaller than 10%. For Pca = 600 MPa, these relative deviations are about 3% whatever L. From pictures of contact areas (see insets of fig. 6), it appears that contact areas are uniformly distributed over the surface, even if the reference length is reduced by a factor 8. Again, this is due to the fact that longer wavelengths have been cut-off by ω_c so that, in the investigated range of L, subdomains have the same distribution of contact areas as the reference one. However, as will be seen below, reducing surface dimensions can either lead to a contact less or more percolating contact (i.e. smaller or larger $\mathbf{K}$ and $\mathbf{D}$).

In figures 13 and 14, we have represented the diagonal terms of $\mathbf{K}$ and $\mathbf{D}$ respectively versus the average contact pressure Pca, for each sampling length L. For small values of L, diagonal terms of $\mathbf{K}$ and $\mathbf{D}$ are increasingly dispersed with Pca. Thus, L has to be large enough to ensure isotropy of the transport properties. Moreover, transport properties of the resized surfaces are randomly distributed around those of the reference surfaces.

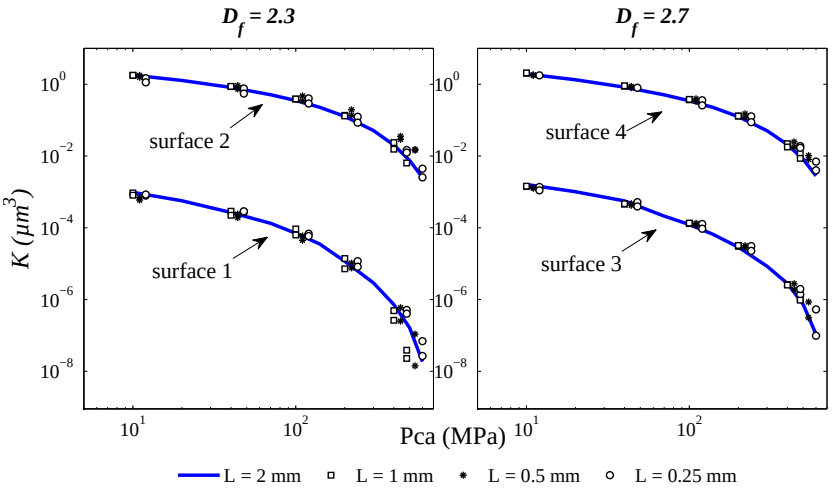

Fig. 13. Effect of sampling length L on the diagonal terms of the transmissivity tensor K. The same symbols are used for the xx and yy components at each value of L -

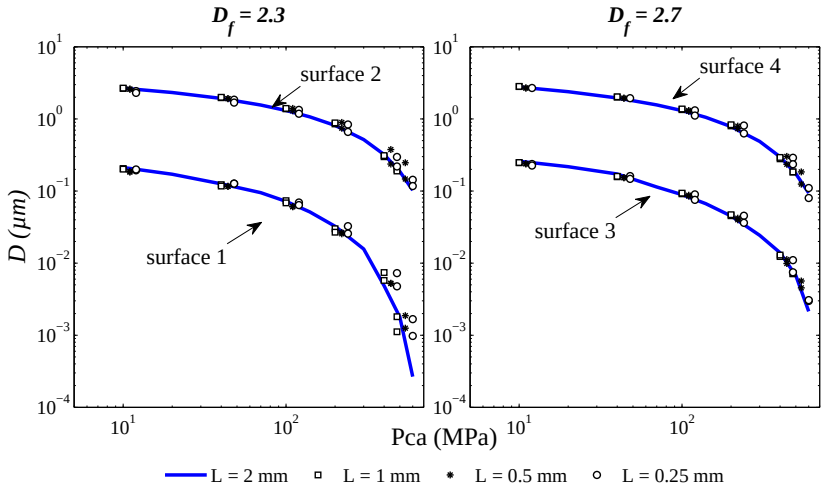

Fig. 14. Effect of sampling length L on the diagonal terms of the diffusivity tensor D. The same symbols are used for the xx and yy components at each value of L -

In figures 15 and 16, we have reported relative errors $\frac{\overline{K_r}-\overline{K}}{\overline{K_r}}$ and $\frac{\overline{D_r}-\overline{D}}{\overline{D_r}}$ for each resized surfaces under consideration. These figures show that relative errors increase with Pca, but confirm that they are not correlated with L. For instance, relative errors obtained on surface 2 are greater in magnitude for $L = 0.5\ mm$ than for $L = 0.25\ mm$ when Pca $\geq 50\ MPa$. As for Δ, transport properties are increasingly sensitive to L when they decrease, i.e. while increasing Pca. For all the sampling lengths considered here, the relative error on the transmissivity does not lead to an over- or under-estimation of $\overline{K}$ greater than a factor 2 ($-100\% \leq \Delta\overline{K}/\overline{K_r} \leq 50\%$) for Pca $\leq 400\ MPa$. In the range of Pca investigated, errors on $\overline{D}$ does not exceed a factor 2, except for surface 1 for which one must keep Pca $\leq 500\ MPa$.

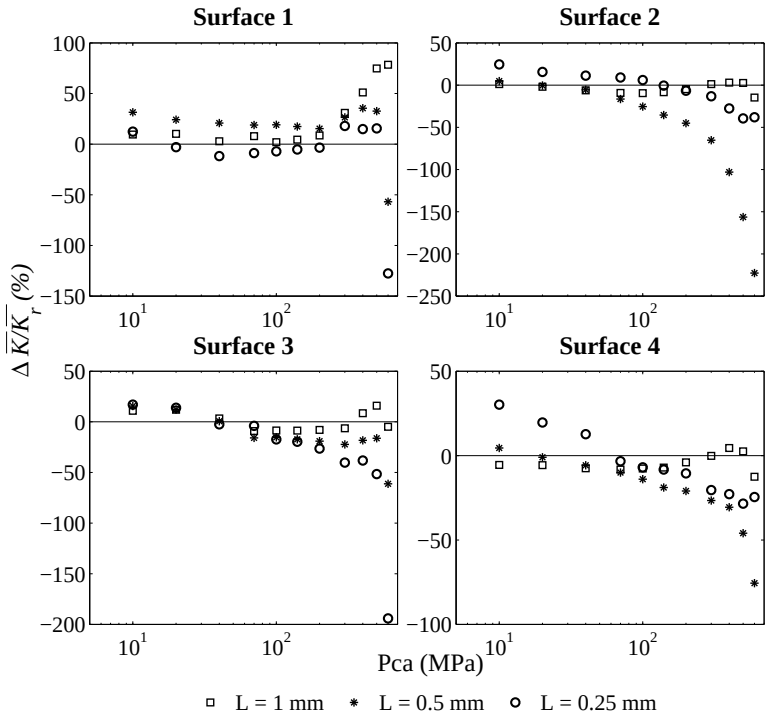

Fig. 15. Relative errors on K with respect to reference surfaces $\frac{\Delta\overline{K}}{\overline{K_r}} = \frac{\overline{K_r}-\overline{K}}{\overline{K_r}}$ for each sampling length under consideration -

4 Conclusion

In this paper, contact between a synthetic fractal surface and a smooth and perfectly rigid plane has been considered. A global deterministic approach to determine surface deformation under load and transport properties of the resulting aperture field has been briefly presented. The effect of sampling variables Δ and L on the estimation of rough surface parameters (D_f and Ra), true contact areas (S_c) and transport properties ($\mathbf{K}$ and $\mathbf{D}$), has been investigated. Both Δ and L were varied by a factor ranging from 2 to 8 with respect to the reference surfaces. As indicated by computational times required to run the whole algorithm, this is a crucial issue that must be considered simultaneously with the expected precision on the estimation of the contact properties. Typically, computational times varies as n^2 (n being the number of data points on the rough surface). To perform this study, four fractal surfaces, considered as references, have been synthesized. They are representative of a wide range of machined surfaces as demonstrated in a companion paper [7]. Since a real surface usually exhibits fractal properties for only a range of frequencies, a cut-off frequency ω_c has been introduced in the power spectrum of synthetic surfaces. This cut-off frequency ensures that dimensions of reference surfaces have been chosen large enough to contain all scales of fractality. Main conclusions of this study are as follows.

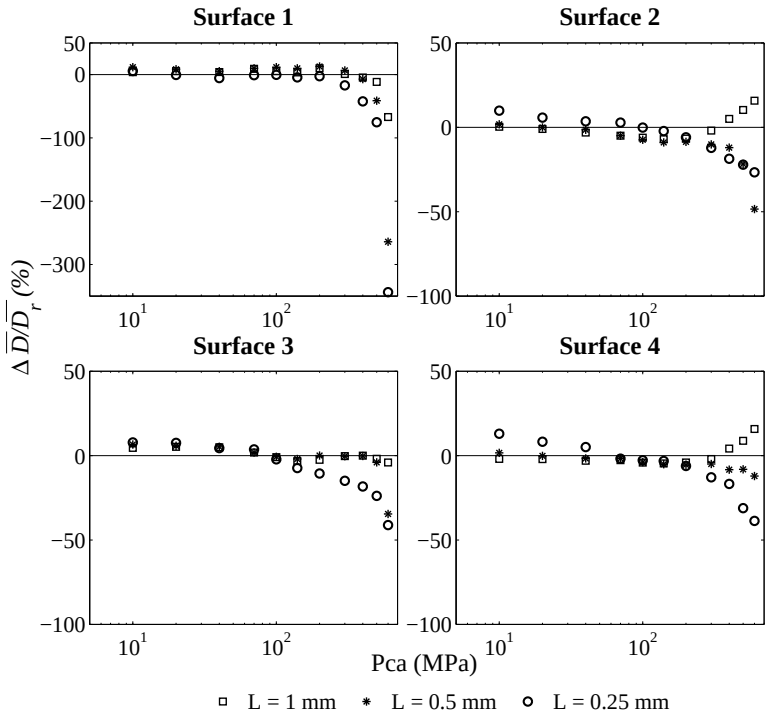

Fig. 16. Relative errors on D with respect to reference surfaces $\frac{\Delta\overline{D}}{\overline{D_r}} = \frac{\overline{D_r}-\overline{D}}{\overline{D_r}}$ for each sampling length under consideration -

The estimation of the fractal dimension D_f remains almost insensitive to the sampling variables provided Δ is kept small compared to ω_c. When this constraint is not satisfied, information contained in the structure function δ becomes insufficient to estimate D_f accurately. Moreover, the effect of the sampling length L is negligible in the investigated range of L. As a consequence, when accuracy on the determination of D_f is to be improved, keeping the amount of data points constant, it is preferable to reduce Δ rather than increasing L.

The arithmetic roughness Ra is much more sensitive to L than to Δ. When a cut-off frequency ω_c is introduced in the power spectrum of the synthetic surfaces, the dependence of Ra to L disappear provided L remains larger than ω_c.

When this last condition is met, longer wavelengths of roughness are cut-off by ω_c, so that distribution of contact spots is homogeneous over the surface. As a consequence, in the range of sampling lengths investigated here, L has very little effect on the estimation of the true contact area S_c. Sensitivity of S_c to Δ becomes significant when Ra is small, i.e. when contact spots are small compared to the block size of the sampling grid, due to a conjugate effect of the representation itself of the contact spots and to a smoothing effect that removes high-frequency content of asperities.

Finally, anisotropy of transport properties can appear as a result of either Δ, which has been chosen too large, or L, which has been chosen too small. Moreover, $\mathbf{K}$ and $\mathbf{D}$ become sensitive to Δ and L at large values of Pca. When significant, under-sampling always leads to an under-estimation of $\mathbf{K}$ and $\mathbf{D}$ and this must be kept in mind if, in practice, leak through a rough contact is to be estimated with such an approach. In contrast, reducing L leads to an under- or over-estimation of $\mathbf{K}$ and $\mathbf{D}$.
For surfaces under consideration, whose properties cover a wide range of D_f and Ra encountered in practice, the impact of Δ and L on $\mathbf{K}$ and $\mathbf{D}$ remains weak. Typically, for the range of variation of Δ and L under investigation in this work, the impact is roughly a factor 2 on $\mathbf{K}$ and $\mathbf{D}$ with respect to the reference surface provided Pca does not exceed 400 MPa. This remains an acceptable estimation for most practical applications if one kepdf in mind the difficulty associated to a precise measurement of these transport properties.

Acknowledgements
Financial support from EDF R&D and CNRS are gratefully acknowledged.

References

[1] R. Zimmerman, G. Bodvarsson, Hydraulic conductivity of rock fractures, Transport in Porous Media 23 (1996) 1–30.

[2] A. Oron, B. Berkowitz, Flow in rock fractures: The local cubic law assumption reexamined, Water Resources Research 34 (11) (1998) 2811–2825.

[3] G. Drazer, J. Koplik, Transport in rough self-affine fractures, Physical Review E 66 (2) (2002) 026303/1–026303/16.

[4] H. Evans, R. Snidle, Analysis of micro-elastohydrodynamic lubrication for engineering contacts, Tribology International 29 (8) (1996) 659–667.

[5] I. Krupka, M. Hartl, The influence of thin film boundary films on real surface roughness in thin film, mixed EHD contact, Tribology International 40 (2007) 1553–1560.

[6] C. Marie, D. Lasseux, H. Zahouani, P. Sainsot, An integrated approach to characterize liquid leakage through metal contact seal, European Journal Mech. and Env. Eng. 48 (2) (2003) 81–86.

[7] C. Vallet, D. Lasseux, P. Sainsot, H. Zahouani, Real versus synthesized fractal surfaces: Contact mechanics and transport properties, Tribology International 42 (2009) 250–259.

[8] A. Nguyen, D. Butler, Correlation-length-based sampling conditions for various engineering surfaces, Measurement Science and Technology 16 (2005) 1813–1822.

[9] K. Stout, L. Blunt, W. Dong, E. Mainsah, N. Luo, T. Mathia, P. Sullivan, H. Zahouani, The Development of Methods for the Characterisation of Roughness in Three Dimensions, Penton Press, London, 2000, 130-174.

[10] B. Mandelbrot, Les Objets Fractals, 3rd Edition, Nouvelle Bibliothèque Scientifique, Flammarion, 1989.

[11] H. Peitgen, D. Saupe, The Science of Fractal Images, Springer-Verlag, New York, 1988.

[12] B. Bhushan, Contact mechanics of rough surfaces in tribology: Multiple asperity contact, Tribology Letters 4 (1998) 1–35.

[13] J. Greenwood, J. Williamson, Contact of nominally flat surfaces, Proc. Roy. Soc. London A295 (1966) 300–319.

[14] P. Nayak, Random process model of rough surfaces in plastic contact, Wear 26 (1973) 305–333.

[15] W. Chang, I. Etsion, D. Bogy, An elastic-plastic model for the contact of rough surfaces, Journal of Tribology 109 (1987) 257–263.

[16] A. Bush, R. Gibson, T. Thomas, The elastic contact of a rough surface, Wear 35 (1975) 87–111.

[17] A. Bush, R. Gibson, G. Keogh, Strongly anisotropic rough surfaces, Journal of Lubrication Technology 101 (1979) 15–20.

[18] A. Majumdar, C. Tien, Fractal characterization and simulation of rough surfaces, Wear 136 (1990) 313–327.

[19] K. Willner, Elasto-plastic normal contact of three-dimensional fractal surfaces using halfspace theory, Journal of Tribology 126 (2004) 28–33.

[20] X. Tian, B. Bhushan, A numerical three-dimensional model for the contact of rough surfaces by variational principle, Journal of Tribology 118 (1996) 33–42.

[21] P. Sainsot, C. Jacq, D. Nélias, A numerical model for elastoplastic rough contact, CMES 3 (4) (2002) 497–506.

[22] K. Johnson, Contact Mechanics, Cambridge University Press, Cambridge, 1985.

[23] C. Jacq, D. Nélias, G. Lormand, D. Girodin, Developement of a three dimensional semi-analytical elastic-plastic contact code, Journal of Tribology 124 (2002) 653–667.

[24] S. Whitaker, The Method of Volume Averaging, Theory and Application of Transport in Porous Media, Kluwer Academic Publishers, 1999.

[25] M. Prat, F. Plouraboué, N. Letalleur, Averaged Reynolds equation for flow between rough surfaces in sliding motion, Transport in Porous Media 48 (2002) 291–313.

[26] M. Quintard, S. Whitaker, Ecoulement monophasique en milieux poreux : Effets des hétérogénéités locales, Journal de Mécanique Théorique et Appliquée 6 (1987) 691–726.

[27] S. Ganti, B. Bhushan, Generalized fractal analysis and its applications to engineering surfaces, Wear 180 (1995) 17–34.

[28] B. Persson, O. Albohr, U. Tartaglino, A. Volokitin, E. Tosatti, On the nature of surface roughness with application to contact mechanics, sealing, rubber friction and adhesion, J. Phys.: Condens. Matter 17 (2005) R1–R62.

[29] W. Chen, Q. Wang, Y. Liu, W. Chen, J. Cao, C. Xia, R. Talwar, R. Lederich, Analysis and convenient formulas for elasto-plastic contacts of nominally flat surfaces: Average gap, contact area ratio, and plastically deformed volume, Tribology Letters 28 (2007) 27–38.

[30] F. Bowden, A review of the friction of solids, Wear 1 (1957) 333–346.

[31] C. Vallet, D. Lasseux, P. Sainsot, H. Zahouani, Numerical determination of sealing performance of a rough contact: Real versus synthetic fractal surfaces, Pressure Vessels and Piping Conference, Chicago, USA, 2008.

[32] C. Marie, D. Lasseux, Experimental leak-rate measurement through a static metal seal, Journal of Fluids Engineering 129 (6) (2007) 799–805.